Journal of Electromyography and Kinesiology 72 (2023) 102808

Contents lists available at ScienceDirect

Journal of Electromyography and Kinesiology

journal homepage: www.elsevier.com/locate/jelekin

Automated spatial localization of ankle muscle sites and model-based estimation of joint torque post-stroke via a wearable sensorised leg garment

Donatella Simonetti [a,*], Maartje Hendriks [b], Joost Herijgers [c], Carmen Cuerdo del Rio [a], Bart Koopman [a], Noel Keijsers [b], Massimo Sartori [a]

[a] Department of Biomechanical Engineering, University of Twente, Enschede, Netherlands
[b] Sint MaartensKlinik, Ubbergen, Netherlands
[c] Twente Medical System Int. (TMSi), Oldenzaal, Netherlands

ARTICLE INFO

Keywords:
Electromyography
Muscle localization
EMG-driven musculoskeletal modeling
Non-negative matrix factorization
Smart wearable technology

ABSTRACT

Assessing a patient's musculoskeletal function during over-ground walking is a primary objective in post-stroke rehabilitation, due to the importance of walking recovery for everyday life. However, the quantitative assessment of musculoskeletal function currently requires lab-constrained equipment, and labor-intensive analyses, which hampers assessment in standard clinical settings. The development of fully wearable systems for the online estimation of muscle–tendon forces and resulting joint torque would aid clinical assessment of motor recovery, it would enhance the detection of neuro-muscular anomalies and it would consequently enable highly personalized treatments.

Here, we present a wearable technology that combines (1) a soft garment for the human leg sensorized with 64 flexible and dry electromyography (EMG) electrodes, (2) a generalized and automated algorithm for the localization of leg muscle sites, and (3) an EMG-driven musculoskeletal modeling framework for the estimation of ankle dorsi-plantar flexion torques.

Our results showed that the automated clustering algorithm could detect muscle locations in both healthy and post-stroke individuals. The estimated muscle-specific EMG envelopes could be used to drive forward person-specific musculoskeletal models and estimate resulting joint torques accurately across all healthy and post-stroke individuals and across different walking speeds ($R2 > 0.82$ and $RMSD < 0.16$).

The technology we proposed opens new avenues for automated muscle localization and quantitative musculoskeletal function assessment during gait in both healthy and neurologically impaired individuals.

1. Introduction

In post-stroke rehabilitation, the recovery of walking capacity is a primary objective (Richards et al., 1993). Optimal gait rehabilitation requires the accurate and continuous assessment of a patient's motor capacity as well as its variation over time. Currently, clinical tools for evaluating gait function post-stroke rely on the visual assessment of a 10-meter walking task (Chan and Pin, 2019; Mehrholz et al., 2007), as well as on the visual assessment of additional simple motor tasks such as walking-by-turning around obstacles or walking on uneven surfaces (Daly et al., 2009; Hafsteinsdóttir et al., 2014). In addition to observational gait function assessment, clinicians may also use 3D gait laboratory analysis to record quantitative data on joint kinematics (using 3D motion capture systems), kinetics (using in-ground force plates), and muscle activation (using surface electromyography - EMG). In this context, advances in musculoskeletal models informed by laboratory-measured EMGs and joint angles (referred to as EMG-driven musculoskeletal models), have enabled the non-invasive estimation of individual muscle–tendon force in both healthy (Durandau et al., 2018) and neurologically impaired individuals (Knarr et al., 2014; Manal et al., 2012), in a variety of dynamic tasks (Tagliapietra et al., 2015), with direct validation at the level of joint torque (Sartori et al., 2014) and stiffness (Cop et al., 2022).

Because human movement emerges from muscle–tendon forces accelerating biological joints, the ability to non-invasively estimate muscle–tendon force in patients would enable monitoring and quantifying a person's walking capacity and design personalized rehabilitation intervention. EMG-driven musculoskeletal models have been largely

* Corresponding author.
E-mail address: d.simonetti@utwente.nl (D. Simonetti).

https://doi.org/10.1016/j.jelekin.2023.102808
Received 18 May 2023; Received in revised form 7 July 2023; Accepted 1 August 2023
Available online 7 August 2023

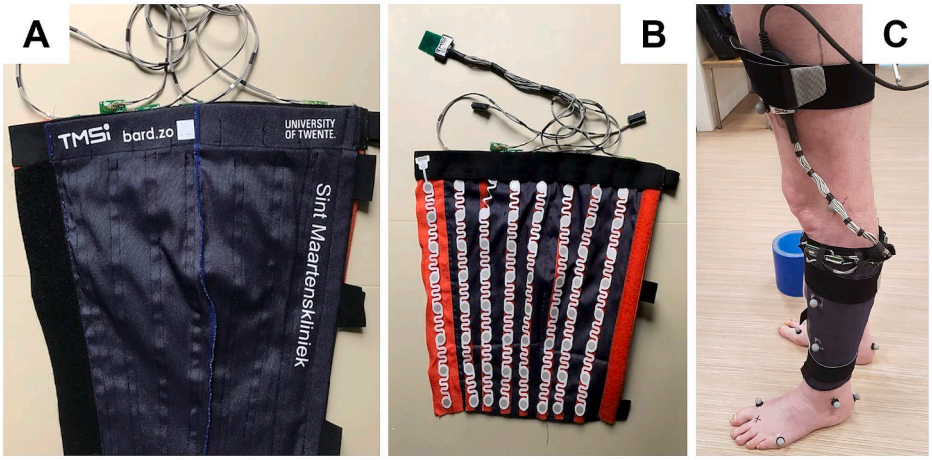

Fig. 1. Beta-series leg garment. (A) External view; (B) inside-view; (C) garment worn by a post-stroke subject.

validated on healthy subjects (Sartori et al., 2014; Cop et al., 2022) and were driven by muscle activations derived by manually placed EMG electrodes. However, manual muscle localization and electrode placement are time-consuming and error-prone procedures (Hermens et al., 2000), hampering daily clinical use of such technologies. These procedures are particularly challenging for post-stroke individuals, who may have undergone structural changes in muscle–tendon tissue composition due to tissue remodeling following stroke (Scherbakov et al., 2013). Moreover, stroke patients often undergo surgeries such as tendon transfer interventions, which alter muscle–tendon unit paths in the attempt of restoring mechanical balance in a given joint (de l'Escalopier et al., 2022). These factors hamper the repeatability, accuracy and time-efficacy of muscle localization in post-stroke individuals, limiting the possibility of estimating underlying muscle–tendon forces via EMG-driven modeling technologies. Therefore, the development of a fully wearable technology could enable quantitative musculoskeletal function analysis outside of fully equipped laboratories such as general clinics and hospitals. We hypothesized that by using EMG-sensorized wearable technologies we could in the future (1) spare the manual human labor required for the muscle localization and electrode placement by enabling a fully automated muscle localization as well as (2) a subsequent extraction of muscle-specific activations in both healthy and post-stroke individuals. Furthermore, we hypothesized that (3) the automatically derived muscle activations could drive a musculoskeletal model and allow the estimation of dorsi-plantar ankle torques in both populations with accuracy comparable to the output of a 3D gait laboratory.

This paper proposes an automated algorithm for the spatial localization of leg muscles from 64 EMG channels embedded in a novel wearable garment as well as subsequent EMG-driven musculoskeletal model-based estimation of ankle muscle–tendon forces and resulting plantar-dorsi-flexion torques during walking in post-stroke individuals. To the best of the authors' knowledge, no previous studies are achieving the proposed target. Factorization or dimensionality reduction algorithms, such as principal component analysis or non-negative matrix factorization (NNMF), were previously applied to process EMG signals measured from neurologically impaired subjects (Ivanenko et al., 2004; Clark et al., 2010) to identify commonalities in multiple specific muscle activations. In our previous work (Simonetti et al., 2022), we demonstrated the ability to automatically extract spatial locations of seven leg muscles from 64 EMG electrodes using an NNMF-based two-step algorithm. However, our previously presented methodology relied on the a priori assumption that a gradient-based NNMF of EMGs can capture contiguous electrode clusters that cover a limited region of the grid.

This assumption did not explicitly enforce locality in the extracted electrode clusters. In the case of large spatially spread co-activation among electrodes, the previous algorithm could potentially lead to the detection of a single large contiguous electrode area potentially covering more than a single muscle. Although this issue did not manifest in our previous study involving healthy subjects, this aspect could become limiting in the case of spastic patients such as post-stroke individuals who display abnormal muscle co-activation (Canning et al., 2000).

With this study, we propose a new garment and develop a new muscle localization algorithm that addresses these limitations and therefore generalizes across musculoskeletal anatomies and neuromuscular control strategies of both healthy subjects and post-stroke individuals.

In the subsequent sections, we first detail the experimental procedures, the newly developed garment, the structure of the new clustering algorithm together with the similarity maps used to enforce contiguity and locality, and the concurrent estimation of musculoskeletal force via EMG-driven modeling (Section 2). Then, we present results on new muscle localization algorithm performances on post-stroke individuals walking at two different speeds. Furthermore, we show how well the automatically derived muscle activations in post-stroke individuals translated in dynamically consistent EMG-driven plantar-dorsi-flexion ankle torque (Section 3). Finally, we discuss the results including study

Table 1
Post-stroke subjects' information.

Subject	Monthssince stroke	Affected side	Dominant side	Type of lesion	FAC*	Garment size
S1	42	left	right	ischemic	5	M
S2	18	left	left	ischemic	5	S
S3	37	left	right	bleeding	5	L
S4	59	left	right	ischemic	4	S
S5	3	right	right	ischemic	5	S
S6	3	left	right	ischemic	4	S
S7	5	left	left	bleeding	5	S

* Functional Ambulation Categories

Table 2
Garment sizes.

Size	Circumpherence (cm) under knee	calf	ankle	length (cm) EMG grid	IED* (cm)
XS	22–27	25–30	17–19	26	3.71
S	26–31	29–34	18–20	26	3.71
M	30–35	32–37	20–23	28	4.0
L	34–39	35–40	23–26	30	4.03

* inter-electrode distance

limitations and future work (Section 4).

2. Methods

2.1. Experimental procedures

The regional medical ethics committee of Eastern Netherlands (METC Oost-Nederland) approved the study procedures (reference number 2022–13658). Seven hemiparetic post-stroke individuals (age = 57 ± 8.7 years, height = 179 ± 5.1 cm, weight = 88.9 ± 16.5 kg) were recruited by the Sint Maartenskliniek (Nijmegen, The Netherlands). After signing an informed consent, EMG, 3D kinetic and kinematic data were recorded during three main tasks: a static standing pose, walking at a self-selected comfortable speed and walking as fast as possible. All participants were instrumented with the wearable garment (Fig. 1) embedded with a grid of 64 EMG electrodes, 37 retro-reflective markers recorded by an optical motion system and performed the task on two floor-embedded force plates. A more detailed description of the experimental setup and procedures is presented in the supplementary material Section 6.1.1.

2.2. Sensorized wearable garment

The textile part of the garment (beta-series prototype) was made, in the outer part, of polyester (90%) and elastomer-filled woven material (10%), while on the inside it was made of white thermo lycra (85% PA, 15% EA). The sleeve was wrapped around the leg and closed using Velcro. The positions of the tibial tuberosity and anterior crest were used as reference points to align the garment consistently across individuals. Moreover, this also prevented having electrodes on prominent bony areas where no muscle activation could be recorded. The sleeve was produced in four sizes related to the different EMG grid lengths and leg circumferences (Table 2).

To enable modularity, custom EMG grids were designed to be interchangeably placed/removed in the inner part of the sleeve via Velcro straps. In this way, the sleeve could be reused while the electrodes could be easily disposed of and, if necessary, re-organized to increase or decrease electrode density in specific parts of the sleeve. The EMG electrodes were made of Ag/AgCl and screen-printed in grids of 8 electrodes each (10 mm in diameter). The grids were made of flexible printed circuit board (PCB) material and designed in three lengths (Table 2). The grids allowed stretch (Table 2) in the longitudinal axis to improve applicability to a wide range of leg lengths. Therefore, specific inter-electrode distance (IED) in the longitudinal axis may be longer or shorter, depending on how the grids were placed into the sleeve.

In our previous work in Simonetti et al. (2022), we developed the first prototype for a textile-embedded 64-channel EMG leg garment. The previous version of our EMG-embedded garment had some drawbacks, such as being difficult to wear due to the compression sock design that included the heel and foot and being available in only one size. The garment also had a fixed number of electrodes that were sewn into the fabric in predetermined locations and were connected to a desktop amplifier through 64 hanging cables. To address these issues, the new garment features an open-sleeve design with velcro straps that can easily wrap around the leg. The sleeve comes in multiple sizes to accommodate various leg lengths and circumferences. Furthermore, we replaced the individual electrodes with 8-EMG grids that can be easily attached and removed to the sleeve using velcro. As a result, we were able to reduce

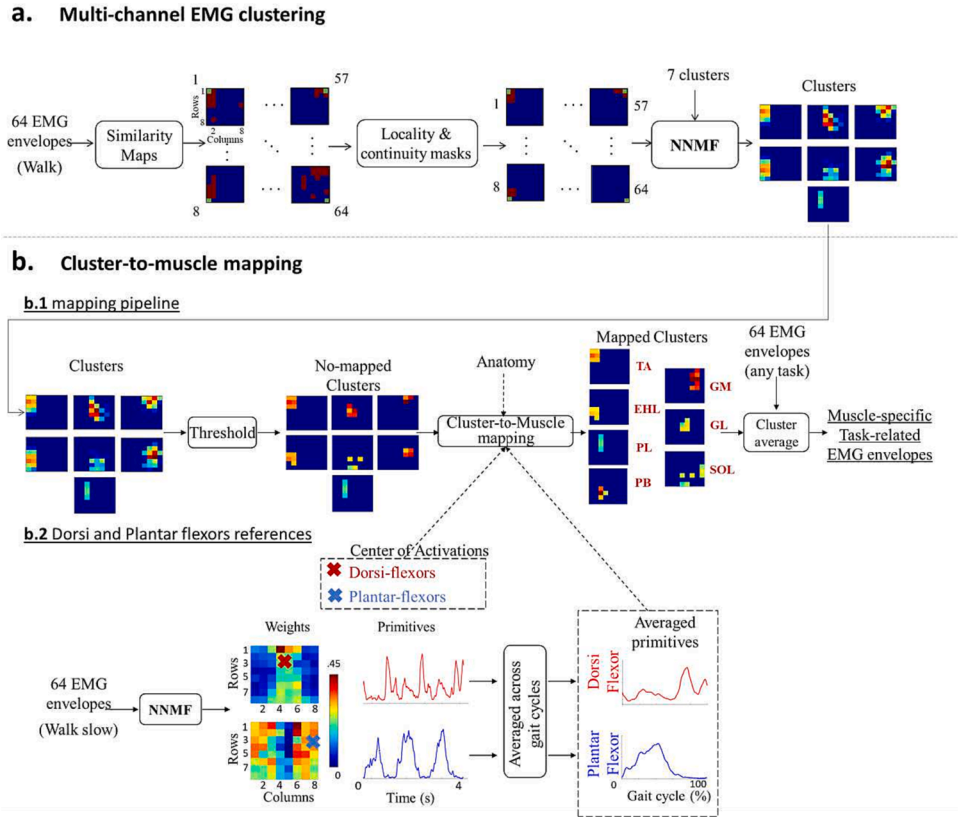

Fig. 2. Schematic of the pipeline including the multi-channel EMG clustering (a) and the clusters-to-muscle mapping (b). The EMG clustering processes the 64 EMG envelopes during a slow walking task to obtain localized and continuous similarity maps. Those are given input to the NNMF to extract seven final clusters. The output of the EMG clustering is used in the cluster-to-muscle mapping to associate each of the extracted clusters to a specific leg muscle and extract average EMG envelopes (b.1). Anatomic information, as well as references dorsi and plantar-flexion, averaged primitives and center of activations are extracted (b.2) and used to map the clusters to specific muscles. Figure b.2 was adapted from (Simonetti et al., 2022).

the number of hanging cables from 64 to 8 while maintaining the same level of functionality.

2.3. Data processing

Signal processing of the raw EMG, kinetic and kinematic data was done on MatlabR (Matlab2020a, MathWorks, Natick (MA), USA).

Kinematic and kinetic data: the data were low-pass filtered at 6 Hz with a zero-lag 2nd order Butterworth filter. Kinetic and kinematic data were used to extract the gait cycles and the post-stroke individuals' walking speed as detailed in the supplementary material 6.1.2.

EMG data: Detection of noisy and silent channels: raw EMG signals were amplified with a gain of 23 (SAGA 64+, TMSi, The Netherlands) and automatically inspected to identify channels with large voltage fluctuations due to movement artifacts as here described. The inspection process encompassed all tasks, including both static standing poses and walking tasks. To remove the drift and the signals' offset, the raw EMG signals were high-pass filtered at 1 Hz with a zero-lag 2nd order Butterworth filter. The standard deviation (std) of each filtered EMG signal and the median among all 64 std values were computed. All channels with std greater than five times the computed median were labeled as noisy. All channels with a std value lower than 0.001 mV were noted as silent, *i.e.*, channels with a flat line signal. All detected noisy and silent channels were set to zero. Re-referencing: raw EMG signals measured from the remaining channels went through re-referencing processing to remove the noise introduced by the noisy channels during the average reference amplification modality (Freeman et al., 2003). In the re-referencing processing, two average reference signals were computed. One for the electrodes underlying dorsi-flexor muscles (first two columns or last two columns of the electrode grids according to the affected side, left or right, respectively) and one for the electrodes underlying plantar-flexor muscles (remaining electrodes). The division between electrodes underlying dorsi- and plantar-flexor muscles to extract the two average reference signals was based on the assumption that the garment and the electrode grids were aligned consistently across individuals (2.2). The re-referenced EMG signals were obtained by subtracting the dorsi- or plantar-flexor average reference signal from the raw EMG signals if belonging to the dorsi- or plantar-flexor groups respectively. Filtering: The re-referenced EMG signals were processed to extract linear envelopes. First, the re-referenced EMG signals were high-pass filtered at 20 Hz using a zero-lag 4th order Butterworth filter and fully rectified. Afterward, the rectified EMG signals went through a moving median filter with a moving window length of 0.16 s. to obtain an equivalent behavior to a low-pass filter with a 6 Hz cut-off frequency (Conforto et al., 1999). The moving median filter allowed removing the remaining spikes due to movement artifacts. Normalization: the resulting linear envelopes were normalized against the maximum linear envelopes' value observed across all performed tasks for each respective channel (Cheung et al., 2009; Neckel et al., 2006).

2.4. Multi-channel EMG clustering

The multi-channel EMG clustering applies NNMF to extract a fixed number of localized and contiguous active areas. The number of active areas was chosen by assuming that there are seven superficial muscles in the human leg (Netter, 2014).

2.4.1. Similarity maps

64 maps of similarity, one for each electrode, were computed using the Euclidean distance and *k*-nearest neighbor clustering (Fig. 2) (Cai et al., 2011). The EMG signals measured from three gait cycles at a comfortable walking speed were used to compute the Euclidean distance between a given electrode envelope (target electrode) and all the 64 EMG envelopes. This was iterated by changing the target electrodes from the first to the 64th. Therefore, 64 sets of 64 Euclidean distance values, *i.e.* 64 similarity maps, were obtained. Then, a *k*-nearest neighbor algorithm ($k = 8$) was applied to each similarity map (Cai et al., 2011) to keep the eight most similar electrodes to each target electrode, *i.e.* the eight lowest Euclidean distances, (Fig. 2.a.2). In each similarity map the target and the eight most close electrodes were set to one and all the other electrodes were set to zero. Eight was chosen since it is the number of electrodes necessary to fully surround a single electrode. In each resulting similarity map, the selected electrodes (target electrode and the eight most similar ones) could all potentially belong to the same cluster. However, the electrodes had to be adjacent (*i.e.*, sharing an edge) and cover a defined, contiguous area in the 8 by 8 grid to belong to

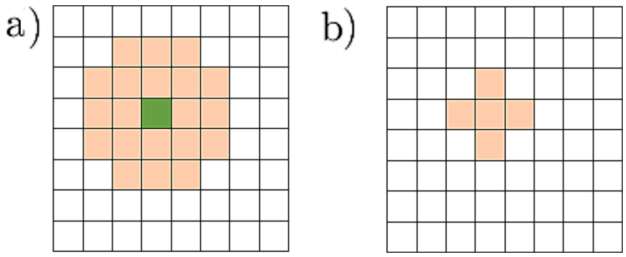

Fig. 3. Masks applied on all 64 similarity maps to ensure locality (a) and continuity (b) among the active channels included in each of the maps.

Table 3
Anatomical information.

Muscle	Function	Electrode position SENIAM	Adopted from SENIAM to grid position for the proposed method
Tibialis anterior	dorsi-flexion	"the electrodes need to be placed at 1/3 on the line between the tip of the fibula and the tip of the medial malleolus"	upper half of the grid
Gastrocnemius lateralis	plantar-flexion	"the electrodes need to be placed at 1/3 of the line between the head of the fibula and the heel"	upper half of the grid and adjacent to the peroneus longus
Gastrocnemius medialis	plantar-flexion	"the electrodes need to be longitudinally on the muscle belly of the lateral head"	upper half of the grid and adjacent to the gastrocnemius lateralis
Soleus	plantar-flexion	"the electrodes need to be placed at 2/3 of the line between the medial condylis of the femur to the medial malleolus"	lower half of the grid
Peroneus longus	Eversion and assistance in plantar-flexion	"the electrodes need to be placed at 25% on the line between the medial condylis of the femur to the medial malleolus"	upper half of the grid and adjacent to the tibialis anterior
Peroneus brevis	Eversion and assistance in plantar-flexion	"the electrodes need to be placed anterior to the tendon of the peroneus longus at 25% of the line from the tip of the lateral malleolus to the fibula-head"	lower half of the grid
Extensor hallucis longus*	dorsi-flexion	"distal two-thirds of the lower leg, between the middle and lower third of tibia"	lower half of the grid, below the tibialis anterior

* The electrode placement was not taken from SENIAM recommendation but following an anatomy book (Marieb and Hoehn, 2007)

the same cluster. This was enforced by sequentially applying two masks on the resulting 64 similarity maps (Fig. 3). To ensure that electrodes within each of the 64 similarity maps covered a limited area of the grid we assumed that the eight most similar electrodes had to be at a maximum distance of two adjacent electrodes from the target electrode (in all directions, mediolateral and distal-proximal). Each similarity map was arranged in an 8 by 8 grid and the mask from Fig. 3.a was applied. The electrode falling outside the first mask was set to zero. To ensure continuity, the remaining electrodes had to be adjacent by creating a contiguous area. The mask from Fig. 3.b was applied and the non-adjacent electrode was set to zero. The resulting similarity maps were 64 sets of 64 values with the target electrodes and the close and adjacent electrodes set to one, while all the remaining electrodes were set to zero.

2.4.2. Factorization of similarity maps

The resulting 64 similarity maps were combined in a single matrix where each row contained a given similarity map. NNMF was applied to the non-negative matrix and decomposed low dimensional features (seven) represented by two non-negative matrices, synergies and weights. The weight matrix contained seven sets of 64 values, giving the seven final local and contiguous active clusters (Fig. 2.a).

2.5. Clusters-to-muscle mapping

Each active cluster resulting from the multi-channel EMG clustering (Section 2.4) was associated with a specific leg muscle (Fig. 2.b.1). We assumed that each active cluster corresponded to an active area of a single muscle. We defined anatomical information (Table 3) based on SENIAM electrode placement recommendations (Stegeman and Hermens, 2007; Hermens et al., 2000).

We defined reference information for plantar and dorsi-flexion functions to discern the muscle function of each active cluster during the mapping process. We applied NNMF on 64 EMG envelopes of three gait cycles at a comfortable walking speed to extract two walking muscle synergies (Ivanenko et al., 2004) related to the leg muscles. The NNMF decomposed the 64 EMG envelopes in primitives and weights related to the dorsi and plantar-flexors muscle groups (Fig. 2.b.2). The primitives were averaged across the three gait cycles to obtain the reference averaged activation profiles for dorsi- and plantar-flexor muscles. Both plantar and dorsi-flexors clusters, were arranged in a 8 x 8 map and the spatial distribution, *i.e.* the position in the medio-lateral and vertical directions, was computed using the center of activation (CoA) as proposed by (van Elswijk et al., 2008). The CoA was a position in an 8 by 8 grid, where each channel was a square pixel of length equal to one, and the distance between the center of two adjacent pixels was equal to one. We used the anatomical information (Table 3), dorsi- and plantar-flexors reference activation profiles and their CoA to associate each cluster to a specific muscle (Fig. 2.b.2). The cluster-to-muscle mapping followed the steps below sequentially:

- The CoA for each active cluster was computed. The EMG envelopes of the active clusters' channels were averaged to obtain the active clusters' envelopes during the three gait cycles at a comfortable walking speed. The active cluster envelopes were averaged across the three gait cycles. Two coefficients of correlation (R) were computed to obtain the similarity between the active cluster averaged envelopes and reference dorsi (R_{df}) and plantar-flexor activations (R_{pf}).
- The active cluster(s) with CoA located in the upper half of the grid, and with R_{df} greater than 0.9 was labeled as tibialis anterior cluster (s).
- The active cluster(s) with CoA located in the lower half of the grid, and with R_{df} greater than 0.8 was labeled as extensor hallucis longus cluster(s).
- The active clusters(s) with CoA located in the lower half of the grid, and with R_{pf} greater than 0.9 was labeled as soleus cluster(s).
- The active cluster with CoA located in the upper half of the grid, and farthest to the tibialis anterior CoA was labeled as gastrocnemius medials cluster.
  - The active cluster with the CoA located in the lower part of the grid was labeled as peroneus brevis.
  - The active cluster with the CoA located higher in the upper part of the grid was labeled as peroneus longus.
  - The remaining cluster(s) was labeled as gastrocnemius lateralis.

Finally, we applied a threshold to extract the most active channels from each labeled cluster. In each cluster, the channels with a weight over 75% of the maximum cluster weight were kept. The weighted average of the normalized EMG envelopes of the kept electrodes for each labeled cluster was considered as the final automatically selected muscle-specific EMG envelope.

2.6. Manual clustering and mapping

To validate (Section 2.9) the automatic cluster selection we manually selected pairs of channels for five specific leg muscles (tibialis anterior, gastrocnemius lateralis and medialis, peroneus longus and soleus). The muscle-specific EMG envelopes derived from manually selected channels were obtained by subtracting the raw monopolar EMG signal of the muscle-specific electrode pairs, and by processing the resulting muscle-specific EMG signals as explained in Section 2.3. We did not manually select a pair of electrodes for the peroneus brevis and the extensor hallucis longus because we experienced major difficulties in the manual detection of these muscle sites for post-stroke individuals.

2.7. Multi-body dynamics pipeline

We analyzed filtered kinetic and kinematic data to obtain joint kinematics and dynamics. Using the open-source software OpenSim (Delp et al., 2007) and marker trajectories from a static task, we scaled a generic musculoskeletal geometry model (gait 2392) to the subject-specific musculoskeletal geometry. From the scaled model, we identified initial person-specific values of optimal fiber length and tendon slack length for each modelled muscle–tendon unit, using a previously developed optimization algorithm (Modenese et al., 2016). Marker trajectories and ground reaction forces (GRFs) during the dynamic tasks were used to solve inverse kinematics (IK) and dynamics (ID) to obtain ankle plantar-dorsi flexion angles and reference torques, respectively.

2.8. EMG-driven musculoskeletal modelling

The alternative path for the estimation of ankle plantar-dorsi flexion torques as well as underlying muscle–tendon force was via EMG-driven musculoskeletal modelling (Durandau et al., 2018; Sartori et al., 2012).

For each subject, we carried out a calibration process to optimize the musculoskeletal model parameters that do not vary linearly across individuals to match each individual's force-generating capacity. This optimization aimed to minimize the mean squared error between the reference and EMG-driven model estimated torques normalized by the variance of the reference torque over the first two gait cycles performed at a comfortable speed. We performed two calibrations for each subject using manually and automatically derived EMG envelopes, respectively. After calibration, the person-specific EMG-driven musculoskeletal model can be used to estimate muscle–tendon force and resulting ankle plantar-dorsi flexion torque using input joint angles and normalized EMG linear envelopes during novel trials that were not used for calibration.

2.9. Validation procedures

For each hypothesis we stated in the introduction we performed a test.

Table 4
Distance (in pixels) between manually and automatically selected muscle-specific clusters' center of activation, for all post-stroke subjects. The number of manually selected electrodes included in the automatically selected clusters is shown in brackets.

Subject	TA	PR	GM	GL	SOL
s01	0.87 (1)	0.38 (2)	1.53 (2)	0.69 (2)	0.38 (2)
s02	0.69 (2)	1.00 (2)	0.59 (1)	1.63 (1)	1.86 (1)
s03	1.21 (2)	1.00 (2)	1.12 (2)	1.05 (2)	1.13 (0)
s04	1.17 (1)	0.41 (2)	0.72 (1)	1.27 (1)	2.17 (0)
s05	1.74 (1)	0.67 (1)	0.82 (2)	1.03 (1)	2.09 (0)
s06	0.51 (2)	1.21 (1)	0.37 (1)	1.53 (1)	1.83 (0)
s07	1.89 (0)	1.53 (0)	1.97 (0)	1.82 (0)	0.34 (2)
	1.15 ± 0.48	0.89 ± 0.39	1.02 ± 0.5	1.29 ± 0.4	1.4 ± 0.73

Test 1 assessed the ability of our algorithm to automatically select muscle-specific electrode clusters with spatial proximity to the ones selected manually. The spatial proximity was computed using two metrics: the number of manually selected muscle-specific electrodes included in the automatically selected muscle-specific cluster, and the Euclidean distance (in pixels) between the manually and automatically selected muscle-specific clusters' CoA.

Test 2 evaluated the shape and amplitude similarity between manually and automatically derived muscle-specific EMG envelopes output from the proposed clustering. Across all subjects, muscles and walking tasks, the coefficient of determination (R^2) for shape similarity, and root mean squared differences (RMSD) for amplitude similarity were computed, along with median and percentiles (25% and 75%), between muscle-specific EMG envelopes derived from automatically and manually selected channels.

Test 1 and Test 2 (see supplementary material Section 6.2), as well as additional tests, were performed on the output of two algorithms, *i.e.*, the one proposed by (Simonetti et al., 2022) and the one here proposed, to assess (1) the ability of both algorithms to extract similar clusters on healthy subjects, (2) to assess the ability of the newly proposed clustering to better identify muscle-specific clusters as limited regions of the grid on post-stroke individuals with respect to the previously developed algorithm.

Test 3 compared reference, manually and automatically derived EMG-driven plantar-dorsi flexion ankle torque for post-stroke individuals walking at two different self-selected speeds. In this way, we further assessed whether our algorithm provided EMG envelopes with the accuracy needed to drive an EMG-driven modeling framework and estimate dynamically consistent ankle torque. The average across all gait cycles of manually and automatically selected EMG-driven torque estimations for both comfortable and fast speeds were compared with the average reference torque using R^2 and normalized root mean square error (NRMSE).

All the retrieved biomechanical signals were compared on a continuous level using statistical parametric mapping (SPM) (Pataky,

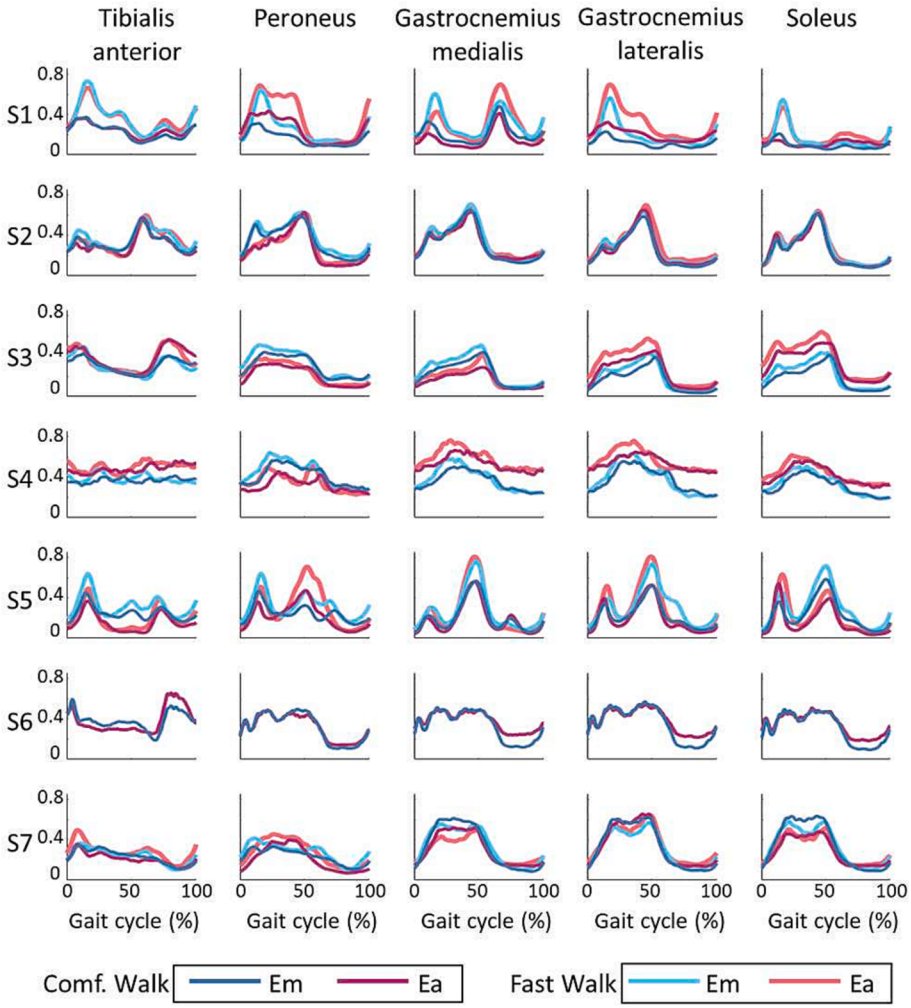

Fig. 4. Manually (E_m - blue lines) and automatically (E_a - red lines) derived normalized EMG envelopes (E). The mean across all gait cycles and for all post-stroke subjects (rows), walking speed (darker colors for comfortable walking speed and lighter colors for fast walking speed) and muscles (columns) are plotted. Data are reported over the gait cycle event with 0% being heel-strike and 100% the following heel strike.

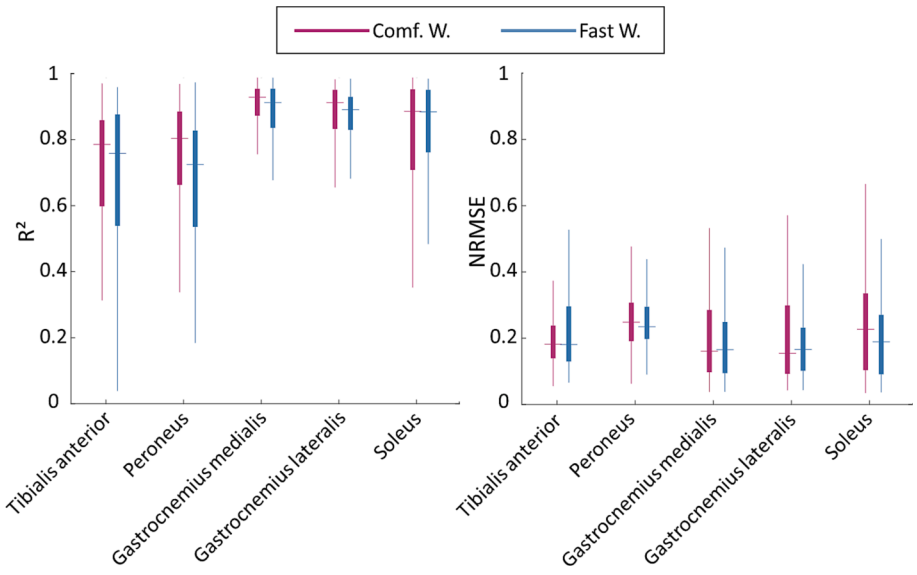

Fig. 5. Box plots displaying the distribution of R^2 and RMSD values computed between manually and automatically derived normalized EMG envelopes of each muscle, across all post-stroke subjects and gait cycles of comfortable (red) and fast (blue) walking. On each box (thick lines), the horizontal line indicates the median value, and the bottom and top edges of the box indicate the 25th and 75th percentiles, respectively. The whiskers (thinner lines) extend the boxes to the most extreme data points not considered outliers.

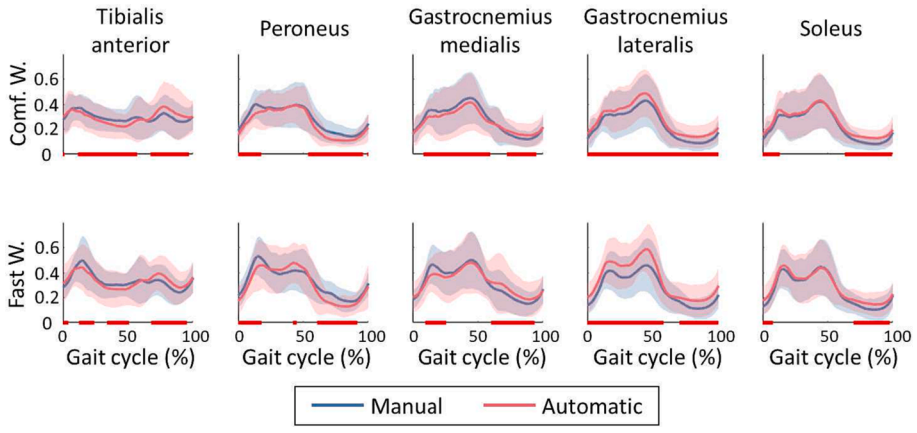

Fig. 6. Manually (E_m - blue lines) and automatically (E_a - red lines) derived normalized EMG envelopes (E). The mean across all gait cycles and post-stroke subjects for all muscles (columns) and for comfortable (first row) and fast (second row) walking are plotted. Data are reported over the gait cycle with 0% being heel-strike and 100% the following heel-strike. On the bottom of each plot, a red horizontal line represents the gait cycle's region where there is a statistical difference ($p < 0.05$) between the automatically and manually derived EMG envelopes waveforms.

2012). SPM was used to compare all gait cycles of manually and automatically derived EMG envelopes in each post-stroke subject and across all subjects during comfortable and fast walking. Similarly, SPM was employed to compare the waveform of manually and automatically derived EMG-driven ankle torque estimates with respect to the reference torque at both comfortable and fast speeds. All SPM analyses were implemented in Matlab using a free open-source package, SPM1D (Pataky, 2012).

3. Results

The number of zeroed channels (noisy and silent channels) across all post-stroke individuals and tasks ranged between 0 and 6 with an average of 2.1 ± 1.9.

Test 1: the results on proximity between manually and automatically selected clusters for and post-stroke individuals are presented in Table 4. The table presented the distance, in % of the garment surface, between the CoA of both manually and automatically selected clusters, and in brackets, the number of manually selected electrodes (two for each leg muscle) that were included in the automatic muscle-specific electrode selection. The distance across all muscles, for post-stroke subjects, ranged between 0.34 and 2.17 pixels with a mean (± std) of 1.15 ± 0.18 pixels.

Test 2: Fig. 4 shows the mean profile of automatically and manually derived EMG normalized envelopes across all gait cycles of comfortable and fast walking tasks for each post-stroke individual and muscle. Fig. 5 displays the distribution R^2 and RMSD values across all gait cycles for each muscle and walking condition. In each box, the central line indicates the median while the bottom and top edges indicate the 25th and 75th percentiles, respectively. The R^2 and RMSD median values for comfortable and fast speeds were ranging between 0.72 and 0.93, and 0.15 and 0.25, respectively. Supplementary Table 5 and supplementary Table 6 report mean (± std) R^2 and RMSD values in detail for post-stroke individuals.

Fig. 6 shows for each muscle and speed, the mean across all gait cycles of all post-stroke subjects for manually and automatically derived EMG envelopes. Furthermore, the gait cycle's regions with a statistical difference ($p < 0.05$) between the two EMG envelope waveforms were highlighted. For comfortable and fast walking the percentage of the gait cycle with a statistical difference was, respectively, 77% and 61% for tibialis anterior, 61% and 52% for peroneus longus, 74% and 50% for gastrocnemius medialis, 100% and 88% a for gastrocnemius lateralis, and 50% and 36% for soleus. A subject-specific significance throughout the gait cycles and for each walking speed is shown in supplementary Fig. 3 and Fig. 4.

Test 3: Fig. 7 displays for all post-stroke subjects the manually and automatically derived EMG-driven ankle torque estimates together with the ankle torque reference profiles across all gait cycles for comfortable and fast walking. Furthermore, the gait cycle's instances where there was a statistical difference ($p < 0.05$) between the reference and both

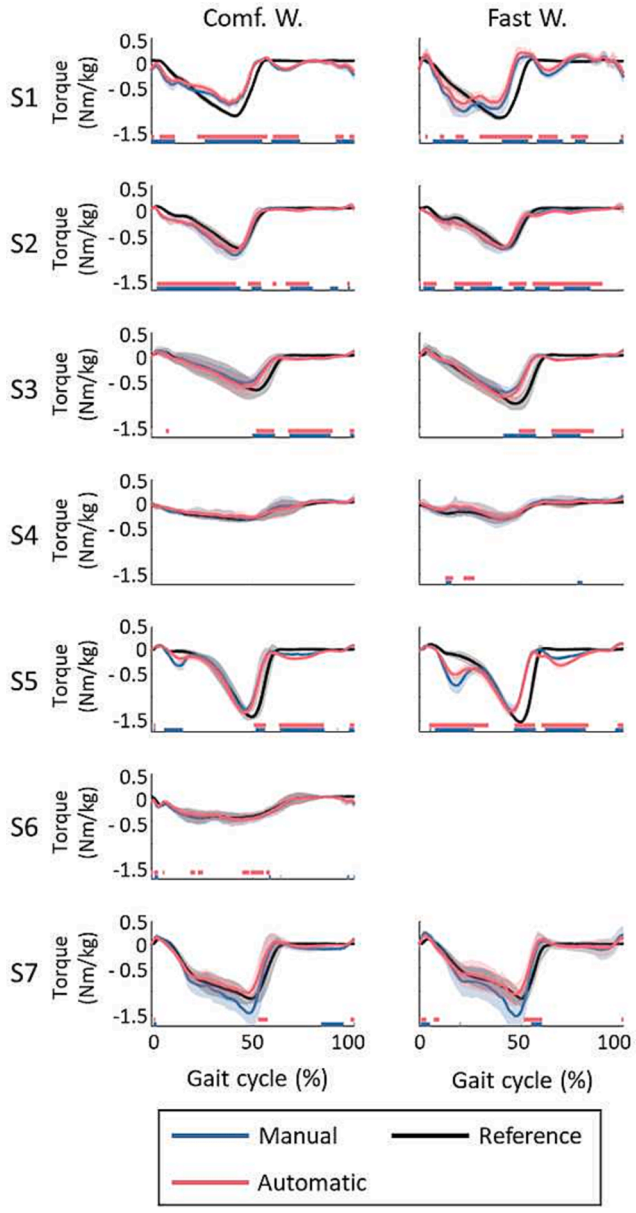

Fig. 7. Ankle joint torques retrieved via inverse dynamics (black lines) and estimated via EMG-driven NMS modeling using both automatically (red lines) and manually derived EMG envelopes (blue lines). The plots report mean (solid lines) and standard deviation (shaded areas) values across all gait cycles for all post-stroke subjects (rows), and for both comfortable (left column) and fast (right column) walking. On the bottom of each plot, a horizontal line represents the gait cycle's region where there is a statistical difference ($p < 0.05$) between the automatically (red) and manually (blue) derived EMG-driven torque estimates with respect to the reference torque.

manually and automatically derived EMG-driven estimated ankle torques were highlighted for each subject. For manually derived EMG-driven ankle torque estimates the percentage of the gait cycle with a statistical difference with respect to the reference torque profile ranged, for comfortable walking, between 0% (subject 4) and 64% (subject 1) with a mean (± std) of 32% ± 24%. For fast walking, the percentage of the gait cycle with a statistical difference ranged between 6% (subject 4) and 55% (subject 5) with a mean (± std) of 35% ± 21%. For automatically derived EMG-driven ankle torque estimates the percentage of the gait cycle with a statistical difference with respect to the reference torque profile ranged, for comfortable walking, between 0% (subject 4) and 64% (subject 1) with a mean (± std) 32% ± 23%. For fast walking, the percentage of the gait cycle with a statistical difference ranged between 6% (subject 4) and 70% (subject 2) with a mean (± std) of 41% ± 23%.

Fig. 8 shows the distribution R^2 and NRMSE values across all gait cycles of all subjects for both walking speeds and for both manually and automatically derived EMG-driven estimates. In each box, the central horizontal line indicates the median while the bottom and top box edges indicate the 25th and 75th percentiles, respectively. The R^2 median values for comfortable and fast speeds were respectively, 0.87 and 0.82 for the manually derived EMG-driven torque estimates, and 0.88 and 0.81 for automatically derived EMG-driven torque estimates. The NRMSE median values for comfortable and fast walking were 0.14 and 0.17, and 0.13 and 0.16 for the manually and automatically derived EMG-driven torque estimates, respectively. Supplementary Table 7 and Table 8 report mean (± std) R^2 and NRMSE values in detail.

4. Discussion

Our study proposed an automated algorithm for the spatial localization of leg muscles from 64 EMG channels embedded in a novel flexible leg garment as well as linked to an EMG-driven musculoskeletal model for the estimation of ankle muscle–tendon forces and resulting plantar-dorsi-flexion torques during walking.

The results showed the ability of the proposed NNMF-based EMG clustering to generalize across healthy and post-stroke populations, as well as the ability to extract the position of the main leg muscles by using 64-electrode activations during a few gait cycles of slow walking (Test 1). Then we used the automatically muscle-specific electrodes derived from the new proposed clustering and obtained electrophysiologically consistent muscle-specific envelopes during all walking speeds (Test 2) for both populations (see supplementary results 6.2). Finally, we evaluated plantar-dorsi flexion ankle torques resulting from a model driven by automatically derived EMG envelopes in post-stroke individuals (Test 3).

We compared our new clustering algorithm against the previously proposed algorithm (Simonetti et al., 2022). When applied on healthy subjects (Supplementary material Section 6.3), we showed that the new clustering extracts muscle-specific clusters with a similar number of comprising electrodes (number of electrodes per muscle-specific cluster between 1 and 10) with respect to (Simonetti et al., 2022). However, when applied on post-stroke individuals, the clustering proposed in this work obtained between 3 and 9 electrodes per muscle-specific cluster and the clustering from (Simonetti et al., 2022) obtained between 1 and 18 electrodes per muscle-specific cluster. Therefore, the new clustering led to more realistic clusters, i.e. limited in a confined area of the grid because part of a single muscle. Therefore, the proposed algorithm is able to generalize from healthy to post-stroke individuals.

Test 1 showed that the proposed clustering and mapping pipelines could extract muscle-specific clusters whose center of activation had a mean Euclidean distance to the manually selected electrode pair varying between 0.9 and 1.8 pixels for both populations (see Table 4 for post-stroke individuals and supplementary Table 3 for healthy subjects). For both healthy and post-stroke individuals, the automatically derived electrodes for the soleus showed the lowest spacial proximity to the manual selection. However, the soleus is a large muscle covering almost the entire calf area (Netter, 2014). The SENIAM sensor placement recommendations (Stegeman and Hermens, 2007), are used to select the manual electrode pairs, restricting the recording area of the soleus to a small fraction of its surface. However, the higher electrode density of the 64-EMG grid can cover a wider area and hence allowing the recording of the soleus activation from the medial and lateral sites.

Test 2 showed that the automatic clustering was able to use 64 electrode activations during a few gait cycles (three) of a single walking task and output electrophysiologically consistent muscle-specific EMG envelopes for all walking tasks in both healthy and post-stroke populations (see Fig. 4). A bigger difference with respect to the manually derived EMG envelopes was always obtained for tibialis anterior and

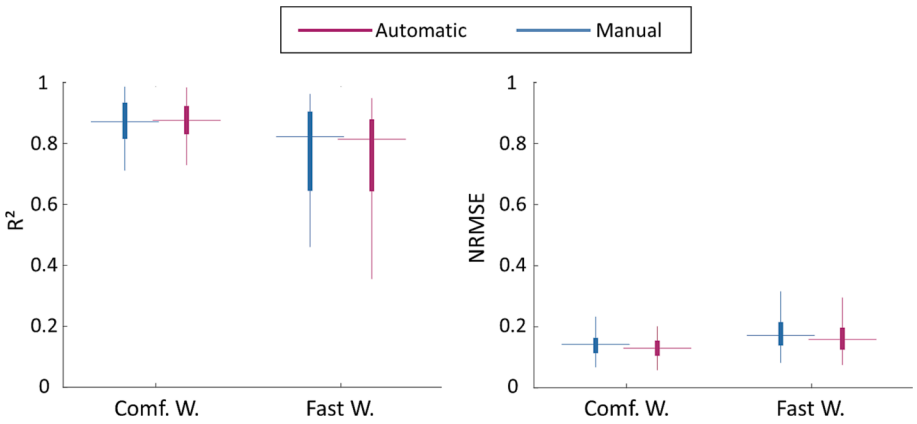

Fig. 8. Box plots displaying the distribution of R^2 and NRMSE values computed between reference ankle torques, and manually (blue) and automatically (red) derived EMG-driven ankle torque estimates across all post-stroke subjects and gait cycles for both comfortable (red) and fast (blue) walking. On each box (thick lines), the horizontal line indicates the median value, and the bottom and top edges of the box indicate the 25th and 75th percentiles, respectively. The whiskers (thinner lines) extend the boxes to the most extreme data points not considered outliers.

peroneus longus in both populations (see Fig. 5, supplementary Table 5 and Table 6 for post-stroke individuals and Table 4 for healthy subjects). The higher variability can result from the increased spatial proximity between these two muscles resulting in possible EMG cross-talk. Future work should assess whether using electrodes with a smaller area and increasing the electrode density in the leg, *i.e.*, smaller IED, can improve the discrimination between the tibialis anterior and the peroneus longus.

Test 3 showed two key results: (1) the EMG clustering and cluster-to-muscle mapping pipelines provided EMG envelopes with the accuracy needed to drive a musculoskeletal modeling framework and estimate dynamically consistent ankle torques. This was visible in the torque estimates during the comfortable speed walking task used for the EMG-driven model calibration as well as for the ankle torque estimates obtained for the unseen (*i.e.*, not used for the EMG-driven model calibration) fast walking task. (2) Even when using abnormal muscle activations from post-stroke individuals, the EMG-driven model output estimated ankle torque with similarity with the reference torque (see Fig. 7). Only a subset of post-stroke participants (subjects 1, 3 and 5) noticeably increased their walking speed across conditions (see supplementary Fig. 1 and supplementary Table 1). For them, both manually and automatically derived EMG-driven ankle torque estimates show an earlier plantar-flexion peak with respect to the reference torque profile (see Fig. 7). The possible shift could be due to the synchronization of motion tracking and EMG systems (see 2.1) during the data recording as well as a different electromechanical delay (EMD) with respect to the other subject showing more impaired walking movements. Grosset et al. (Grosset et al., 2009) stated that the higher the stiffness is in the musculotendinous units, the lower the EMD, and *vice versa. Son et al. (Son and Rymer, 2021) revealed that the EMD in paretic muscles was significantly longer than in non-paretic muscles. Future works should quantify the delay introduced by the hardware synchronization trigger as well as compute a subject-specific EMD delay and investigate how this affects the EMG-driven model outcome.*

In contrast to our previous work (Simonetti et al., 2022), the sensorized garment and the EMG clustering technique were generalized to facilitate their use on neurologically impaired individuals. First, the straightforward application process of the sensorized garment allowed for a simple setup. Secondly, the computation of similarity maps together with *k*-nearest neighbor clustering and the applied masks (see Section 2.4) enforced the extraction of localized and continuous clusters in healthy subjects as well as in post-stroke individuals with different degrees of impairment (Table 1). However, the newly proposed methodology still relies on the *a priori assumption that post-stroke individuals control the leg muscles through two walking muscle synergies (Ivanenko et al., 2006; Cappellini et al., 2006) and that there are seven active superficial muscles in the leg.*

This study includes limitations that should be addressed in future works. The automatically derived EMG envelopes were compared with manually derived EMG envelopes. The manual selection included pairs of electrodes within the garment separated by a variable distance (2) while the SENIAM recommendation suggests 2.0 cm IED in bipolar configuration and De Luca et al. (De Luca et al., 2012) suggested that an IED of 1.0 cm is optimal to reduce cross-talk during walking. Furthermore, the manual electrode selection can be affected by a systematic error (Hermens et al., 2000), even more, when the muscle belly is atrophied or not as evident as in healthy individuals. This study included seven post-stroke individuals for the initial validation of a smart wearable technology. Future work should include more subjects to enhance the statistical power to the presented study and further assess the generalization capacity of our proposed methodology. Furthermore, the healthy and post-stroke populations involved in this work presented differences in age and BMI, thereby limiting the comparison of results. To ensure that our methodology is generalizable across ages and body compositions, future work should include more participants in both populations with a more diverse range of ages and BMI. Additionally, future research should focus on assessing the clinical relevance and practical application of our results. In this study, the EMG-driven modeling was validated at the level of joint torque. However future work should include validation also at the level of muscle forces. The study showed the capacity of the developed technology to be suitable for a specific impaired population, *i.e.*, post-stroke individuals. This opens the possibility to test its efficacy on diverse populations, such as SCI patients or injured athletes. The clustering and mapping pipelines were applied to a specific limb. Future work should generalize across different body parts, including the upper leg as well as the upper limb. Furthermore, the present study presented a technology not yet fully portable. Future studies should remove the need for laboratory-based technologies, such as force plates and camera-based tracking systems, and employ wearable sensors for kinetics and kinematics to go toward fully wearable and portable technology.

5. Conclusion

We show how to go from a multi-channel EMG-sensorized garment to ankle plantar-dorsi flexion torque by means of automatic NNMF-based EMG clustering and EMG-driven modeling techniques. The developments made in this study open new avenues for fast and quantitative musculoskeletal function assessment in post-stroke individuals and potentially for any injured population.

Declaration of Competing Interest

The authors declare that they have no known competing financial interests or personal relationships that could have appeared to influence the work reported in this paper.

Acknowledgment

The work was supported by EFRO OP Oost GUTs (20913301). The smart garment was developed in collaboration with TMSi (Oldenzaal, Netherlands) and Bard.zo Proad (Ommen, Netherlands).

Appendix A. Supplementary material

Supplementary data associated with this article can be found, in the online version, at https://doi.org/10.1016/j.jelekin.2023.102808.

References

Cai, D., He, X., Han, J., Huang, T.S., 2011. Graph regularized nonnegative matrix factorization for data representation. IEEE Trans. Pattern Anal. Mach. Intell. 33, 1548–1560. https://doi.org/10.1109/TPAMI.2010.231.

Canning, C.G., Ada, L., O'Dwyer, N.J., 2000. Abnormal muscle activation characteristics associated with loss of dexterity after stroke. J. Neurol. Sci. 176, 45–56. https://doi.org/10.1016/S0022-510X(00)00305-1.

Cappellini, G., Ivanenko, Y.P., Poppele, R.E., Lacquaniti, F., 2006. Motor patterns in human walking and running. J Neurophysiol 95, 3426–3437. https://doi.org/10.1152/jn.00081.2006.

Chan, W.L., Pin, T.W., 2019. Reliability, validity and minimal detectable change of 2-minute walk test, 6-minute walk test and 10-meter walk test in frail older adults with dementia. Exp. Gerontol. 115, 9–18. https://doi.org/10.1016/J.EXGER.2018.11.001.

Cheung, V.C.K., Piron, L., Agostini, M., Silvoni, S., Turolla, A., Bizzi, E., 2009. Stability of muscle synergies for voluntary actions after cortical stroke in humans. In: Proceedings of the National Academy of Sciences doi:10.1073/pnas.0910114106.

Clark, D.J., Ting, L.H., Zajac, F.E., Neptune, R.R., Kautz, S.A., 2010. Merging of healthy motor modules predicts reduced locomotor performance and muscle coordination complexity post-stroke. Journal of neurophysiology. https://doi.org/10.1152/jn.00825.2009.

Conforto, S., D'Alessio, T., Pignatelli, S., 1999. Optimal rejection of movement artefacts from myoelectric signals by means of a wavelet filtering procedure. J. Electromyogr. Kinesiol. 9, 47–57. https://doi.org/10.1016/S1050-6411(98)00023-6.

Cop, C.P., Schouten, A.C., Koopman, B., Sartori, M., 2022. Electromyography-driven model-based estimation of ankle torque and stiffness during dynamic joint rotations in perturbed and unperturbed conditions. J. Biomech. 145, 111383. https://doi.org/10.1016/J.JBIOMECH.2022.111383.

Daly, J.J., Nethery, J., McCabe, J.P., Brenner, I., Rogers, J., Gansen, J., Butler, K., Burdsall, R., Roenigk, K., Holcomb, J., 2009. Development and testing of the Gait Assessment and Intervention Tool (G.A.I.T.): A measure of coordinated gait components. J. Neurosci. Methods 178, 334–339. https://doi.org/10.1016/J.JNEUMETH.2008.12.016.

De Luca, C.J., Kuznetsov, M., Gilmore, L.D., Roy, S.H., 2012. Inter-electrode spacing of surface EMG sensors: reduction of crosstalk contamination during voluntary contractions. Journal of biomechanics 45, 555–561. https://doi.org/10.1016/J.JBIOMECH.2011.11.010.

Delp, S.L., Anderson, F.C., Arnold, A.S., Loan, P., Habib, A., John, C.T., Guendelman, E., Thelen, D.G., 2007. OpenSim: open-source software to create and analyze dynamic simulations of movement. IEEE transactions on bio-medical engineering 54, 1940–1950. https://doi.org/10.1109/TBME.2007.901024.

Durandau, G., Farina, D., Sartori, M., 2018. Robust Real-Time Musculoskeletal Modeling Driven by Electromyograms. IEEE Trans. Biomed. Eng. 65, 556–564. https://doi.org/10.1109/TBME.2017.2704085.

van Elswijk, G., Kleine, B.U., Overeem, S., Eshuis, B., Hekkert, K.D., Stegeman, D.F., 2008. Muscle imaging: Mapping responses to transcranial magnetic stimulation with high-density surface electromyography. Cortex 44, 609–616. https://doi.org/10.1016/J.CORTEX.2007.07.003.

Freeman, W.J., Holmes, M.D., Burke, B.C., Vanhatalo, S., 2003. Spatial spectra of scalp EEG and EMG from awake humans. Clin. Neurophysiol. 114, 1053–1068. https://doi.org/10.1016/S1388-2457(03)00045-2.

Grosset, J.F., Piscione, J., Lambertz, D., Pérot, C., 2009. Paired changes in electromechanical delay and musculo-tendinous stiffness after endurance or plyometric training. Eur. J. Appl. Physiol. 105, 131–139. https://doi.org/10.1007/S00421-008-0882-8.

Hafsteinsdóttir, T.B., Rensink, M., Schuurmans, M., 2014. Clinimetric Properties of the Timed Up and Go Test for Patients With Stroke: A Systematic Review. https://doi.org/10.1310/TSR2103-197.

Hermens, H.J., Freriks, B., Disselhorst-Klug, C., Rau, G., 2000. Development of recommendations for SEMG sensors and sensor placement procedures. J. Electromyogr. Kinesiol. 10, 361–374. https://doi.org/10.1016/S1050-6411(00)00027-4.

Ivanenko, Y.P., Poppele, R.E., Lacquaniti, F., 2004. Five basic muscle activation patterns account for muscle activity during human locomotion. J. Physiol. 556, 267–282. https://doi.org/10.1113/jphysiol.2003.057174.

Ivanenko, Y.P., Poppele, R.E., Lacquaniti, F., 2006. Motor control programs and walking. Neuroscientist 12, 339–348. https://doi.org/10.1177/1073858406287987.

Knarr, B.A., Reisman, D.S., Binder-Macleod, S.A., Higginson, J.S., 2014. Changes in predicted muscle coordination with subject-specific muscle parameters for individuals after stroke. Stroke Research and Treatment 2014. https://doi.org/10.1155/2014/321747.

de l'Escalopier, N., Voisard, C., Michaud, M., Moreau, A., Jung, S., Tervil, B., Vayatis, N., Oudre, L., Ricard, D., 2022. Evaluation methods to assess the efficacy of equinovarus foot surgery on the gait of post-stroke hemiplegic patients: A literature review. Frontiers in Neurology 13. https://doi.org/10.3389/fneur.2022.1042667.

Manal, K., Gravare-Silbernagel, K., Buchanan, T.S., 2012. A real-time EMG-driven musculoskeletal model of the ankle. Multibody Sys.Dyn. https://doi.org/10.1007/s11044-011-9285-4.

Marieb, E.N., Hoehn, K., 2007. Human Anatomy & Physiology. Pearson education.

Mehrholz, J., Wagner, K., Rutte, K., Meißner, D., Pohl, M., 2007. Predictive Validity and Responsiveness of the Functional Ambulation Category in Hemiparetic Patients After Stroke. Arch. Phys. Med. Rehabil. 88, 1314–1319. https://doi.org/10.1016/j.apmr.2007.06.764.

Modenese, L., Ceseracciu, E., Reggiani, M., Lloyd, D.G., 2016. Estimation of musculotendon parameters for scaled and subject specific musculoskeletal models using an optimization technique. J. Biomech. 49, 141–148. https://doi.org/10.1016/J.JBIOMECH.2015.11.006.

Neckel, N., Pelliccio, M., Nichols, D., Hidler, J., 2006. Quantification of functional weakness and abnormal synergy patterns in the lower limb of individuals with chronic stroke. J. NeuroEng. Rehabil. https://doi.org/10.1186/1743-0003-3-17.

Netter, F.H., 2014. Atlas of Human Anatomy, Professional Edition E-Book: including NetterReference. com Access with full downloadable image Bank. Elsevier health sciences.

Pataky, T.C., 2012. One-dimensional statistical parametric mapping in Python. Comput. Methods Biomech. Biomed. Eng. 15, 295–301. https://doi.org/10.1080/10255842.2010.527837.

Richards, C.L., Malouin, F., Wood-Dauphinee, S., Williams, J.I., Bouchard, J.P., Brunet, D., 1993. Task-specific physical therapy for optimization of gait recovery in acute stroke patients. Arch. Phys. Med. Rehabil. 74, 612–620. https://doi.org/10.1016/0003-9993(93)90159-8.

Sartori, M., Farina, D., Lloyd, D.G., 2014. Hybrid neuromusculoskeletal modeling to best track joint moments using a balance between muscle excitations derived from electromyograms and optimization. J. Biomech. 47, 3613–3621. https://doi.org/10.1016/J.JBIOMECH.2014.10.009.

Sartori, M., Reggiani, M., Farina, D., Lloyd, D.G., 2012. EMG-Driven Forward-Dynamic Estimation of Muscle Force and Joint Moment about Multiple Degrees of Freedom in the Human Lower Extremity. PLoS ONE 7, e52618. https://doi.org/10.1371/journal.pone.0052618.

Scherbakov, N., Von Haehling, S., Anker, S.D., Dirnagl, U., Doehner, W., 2013. Stroke induced Sarcopenia: Muscle wasting and disability after stroke. Int. J. Cardiol. 170, 89–94. https://doi.org/10.1016/J.IJCARD.2013.10.031.

Simonetti, D., Koopman, B., Sartori, M., 2022. Automated estimation of ankle muscle EMG envelopes and resulting plantar-dorsi flexion torque from 64 garment-embedded electrodes uniformly distributed around the human leg. J. Electromyogr. Kinesiol. 67, 102701. https://doi.org/10.1016/J.JELEKIN.2022.102701.

Son, J., Rymer, W.Z., 2021. Longer electromechanical delay in paretic triceps surae muscles during voluntary isometric plantarflexion torque generation in chronic hemispheric stroke survivors. J. Electromyogr. Kinesiol. 56, 102475. https://doi.org/10.1016/J.JELEKIN.2020.102475.

Stegeman, D.F., Hermens, H.J., 2007. Standards for surface electromyography: the European project Surface EMG for non-invasive assessment of muscles (SENIAM). In: Enschede: Roessingh Research and Development, 10, pp. 8–12.

Tagliapietra, L., Vivian, M., Sartori, M., Farina, D., Reggiani, M., 2015. Estimating EMG signals to drive neuromusculoskeletal models in cyclic rehabilitation movements. In: Proceedings of the Annual International Conference of the IEEE Engineering in Medicine and Biology Society. Institute of Electrical and Electronics Engineers Inc., pp. 3611–3614. https://doi.org/10.1109/EMBC.2015.7319174